Phase-field simulation and machine learning study of the effects of elastic and plastic properties of electrode and solid polymer electrolyte on the suppression of Li dendrite growth

Yao Ren[1], Kena Zhang[1], Yue Zhou[2], and Ye Cao[1,*]

[1]Department of Materials Science and Engineering, University of Texas at Arlington, Arlington, TX 76019, USA.

[2]Department of Electrical Engineering and Computer Science, South Dakota State University, Brookings, SD, 57007

[*] Corresponding Author: Email: ye.cao@uta.edu

Abstract

Lithium (Li) dendrite growth in Li batteries is a long-standing problem which causes critical safety concerns and severely limits the advancement of rechargeable Li batteries. Replacing conventional liquid electrolyte with solid electrolyte of high mechanical strength and rigidity has become a potential approach to inhibiting the Li dendrite growth. However, there still lacks accurate understanding on the role of the mechanical properties of the metal electrode and the solid electrolyte in the Li dendrite growth. In this work, we develop a phase-field model coupled with the elasto-plastic deformation to investigate the Li dendrite growth and its inhibition in the cell. Different mechanical properties, including the elastic modulus and the initial yield strength of both the metal electrode and the solid electrolyte are explored to understand their independent roles in the inhibition of Li dendrite growth. High-throughput phase-field simulations are

performed to establish a database of relationships between the aforementioned mechanical properties and the Li dendrite morphology, based on which a compressed-sensing machine learning model is trained to derive interpretable analytical correlations between the key material parameters and the dendrite morphology, as described by the dendrite length and area ratio. It is revealed that the Li dendrite can be effectively inhibited by the electrolytes of high elastic modulus and initial yield strength. Meanwhile, the role of the yield strength of Li metal is also critical when the yield strength of the electrolyte becomes low. This work provides a fundamental understanding of the dendrite inhibition by the mechanical suppression, and demonstrates a computational data-driven methodology to potentially guide the electrode and electrolyte materials selection for better inhibition of the dendrite growth.

Keywords: phase-field simulation, lithium dendrite inhibition, high-throughput calculation, machine learning, elasto-plasticity

1. Introduction

The ever-growing demand of wearable and mobile electronic devices, electric vehicles, grid-scale electrical storage, and other energy storage systems requires the advancement of lithium-ion (Li-ion) batteries of high energy density and improved safety and stability[1,2]. One of the most promising approach is to replace the existing graphite anodes with the lithium (Li) metal anodes, which has the highest theoretical capacity (3860 mAh/g), low density (0.53g/cm^3), and lowest negative electrochemical potential (-3.04V vs. standard hydrogen electrode) [3,4]. However, a critical issue that

impedes the wide application of Li metal battery is the uncontrollable Li electrodeposition in the form of dendrites or filaments. These needle- or branch-like dendrites can eventually penetrate the separator of the cell, which creates serious problems such as lowered Coulombic efficiency, large mechanical deformation of the electrodes, reduced battery cycle life, and catastrophic internal short circuit[5,6].

Multiple approaches have been proposed to inhibit the Li dendrite growth[7,8]. Among them, the mechanical suppression on dendrites using solid electrolyte (SE) of high mechanical strength and good ionic conductivity is one of the most promising methods[9,10]. Numerous studies have been made to understand the Li dendrite suppression effect by the solid inorganic (ceramic) electrolytes[11,12], solid polymer electrolytes[10], and the ceramic/polymer composite electrolytes[13–16]. A seminal model related to the elastic effect in Li battery was done by Monroe and Newman, who discovered that the Li dendrite can be stabilized when the shear modulus of the electrolyte is at least twice as that of Li metal[17]. However, recent findings indicated that the Monroe-Newman theory cannot explain all the phenomena in Li dendrite growth. For example, inorganic ceramics, such as $Li_7La_3Zr_2O_{12}$ (LLZO)[18], β-Li_3PS_4[19], and $Li_2(OH)_{0.9}F_{0.1}Cl$[20], which showed extremely high elastic (and shear) modulus (~10^2 GPa), still suffered from Li dendrite growth. On the other hand, soft SEs with very low elastic modulus (such as rubber, E= 0.4 MPa) can still suppress Li dendrite growth over long cycling time[21,22].

One of the reasons that could cause these discrepancies arise from the complicated mechanical properties of Li metal anode. Monroe-Newman's theory is based on the

linear elasticity theory and ignores the plasticity effect. Since Li metal possess a relatively low melting temperature (180°C) and yield strength (0.7MPa for bulk Li metal), plastic deformation could occur during Li dendrite growth[23]. More importantly, the yield strength of Li metal (σ_y^m) is strongly dependent on the Li grain size[18,24], temperature[25], and the strain rate[26]. It has been reported that σ_y^m could increase from ~0.7MPa to 10^1~10^2 MPa when the Li grain diameter decreases down to several microns[25]. Li anode could also demonstrate substantial viscoplastic effect[27,28], with its yield strength (σ_y^m) varying from 0.3MPa to 10MPa when the current density (and thus the strain rate) changes from 1A/m^2 to 100A/m^2 [29]. Therefore, it is possible that Li anode might exhibit a large variation in σ_y^m during the nucleation and growth of Li dendrite. For a better inhibition effect of the Li dendrite growth, it should balance the bulk strength for supporting the required stack stress[30] and dendrite strength for avoiding the Li whisker inserting into electrolyte[31].

Another major reason is the existence of local defects and the complicated microstructure in the solid electrolyte. Pre-existing defects such as pores and cracks are common in ceramic SEs. Li plating prefer to infiltrate these defects due to a local electric field enhancement, which produces crack-tip stress that could further drive crack propagation, causing more Li dendrite penetration[19,32]. Inhomogeneous microstructure, such as surfaces and grain boundaries (GBs) also play key roles in the Li plating. Yu *et al.* reported up to 50% reduction in elastic modulus at GB regions of LLZO than in the bulk[33], and the additional electronic states in the vicinity of the GB regions[34], which explains why Li dendrite prefer to grow along the GBs[35]. On the other

hand, polymer SE is usually embedded with inorganic fillers (such as oxides) to increase its overall mechanical stiffness for Li dendrite suppression[36]. Their elastic moduli could vary from ~10^{-2} to ~10 GPa and their yield strength from ~10^{-1} to 10^{2} MPa, respectively [37]. Thus, the existences of local defects and the microstructure inhomogeneity significantly influence the overall mechanical properties of the solid electrolyte, which would further influence the Li dendrite growth behaviors. Therefore, a fundamental understanding of the mechanical properties of both Li metal and the solid electrolyte, and their influences on the Li dendrite growth is urgently needed.

Several theoretical models have also been developed to understand the Li dendrite growth mechanism in solid state electrolyte. Following the pioneer work by Monroe and Newman[17], Barai *et al.* employed a similar morphological domain for dendrite initiation[38], and studied the external pressure, ionic conductivity, elastic properties, and solid electrolyte grain structure on the Li anode stability[39,40]. Ahmad *et al.* postulated a general criteria for the stability of electrodeposition at electrode-electrolyte interface (EEI) by considering the density change of Li metal[41]. However, these analytical models assumed a fixed electrode-electrolyte interface, and compared the current density at the interface "peak" and "valley" as the criteria to determine the Li dendrite growth. Atomic scale molecular dynamics (MD) simulation and first-principles calculations have also been employed to investigate the grain boundary softening effect[33] and the electronic density of states at the SE surface[35]. Nevertheless, these simulations did not consider the real morphology of the Li metal dendrite, which could play an important role in determining the Li dendrite growth behaviors.

Phase-field simulation has emerged as a powerful tool to model the microstructure evolution in various material systems. In the phase-field model, the interface between different phases is treated as a diffuse interface, which is characterized by an order parameter that varies its value continuously from one phase (the electrode in this study) to another (electrolyte). The interfacial motion can thus be explicitly tracked by the evolution of that order parameter. Several phase-field models have recently been developed to simulate the Li dendrite growth[42–44], and study the effects of initial anode surface morphology[45], temperature[46], thermal shock healing[47], elastic strain[48], and grain structure[49] on the Li anode stability. However, very few models consider the effects of both elastic stress and the plastic yielding during the Li electrodeposition on the Li dendrite growth. While the negligence of the elastic and plastic effects seems valid for liquid electrolyte, in SE the mechanical stress and the Li plastic yielding play critical roles during Li plating process and should NOT be ignored. Although some recent works considered the effects of elasto-plastic deformation, due to the Li filament growth on a soft or stiff matrix[50], the inverse mechanism of elastic and plastic deformation on the elastic energy density, and the resulting Li dendrite growth has not been incorporated.

In this paper, we developed a phase-field model coupled with an elasto-plastic deformation model to investigate the impact of elastic and plastic deformation of Li metal and solid electrolyte on the Li dendrite growth. Three key mechanical properties, i.e., the initial yield strengths of Li metal and the electrolyte, and the elastic modulus of the electrolyte are selected and their effects on the Li dendrite growth are systematically

studied to establish a general understanding of their inhibitory effects. Based on this, we select two characteristic features of the Li dendrite morphology, i.e., the length of the main branch and the area ratios of the side growth, and perform high-throughput phase-field simulations by parameterizing the above three key mechanical properties to create a mechanical property – dendrite morphology database. Machine learning is then performed to construct a predictive model for the Li dendrite characteristic features as a function of the above three mechanical properties. Finally, we study the effect of the elastic modulus of the metal electrode on the dendrite growth, and provide some guidance for the design of other metal anode batteries.

2. Method

2.1 Electrochemical Model

Our simulation system consists of a standard half-cell which contains a Li anode and a solid polymer electrolyte. We assume that the anode is composed of pure Li metal, while the polymer electrolyte consists of the positively charged Li-ion (Li^+) and negatively charged anion (A^-), the latter of which is an effective charge for all the remaining charges. It is further assumed that Li^+ is the only mobile ion, while electrons (e^-) are always provided on the anode surface due to their relatively high mobility. We do not consider other types of cations or anions, and the temperature is assumed to be uniform and not changing with time. For simplify, a solid-electrolyte-interface (SEI) layer is not explicitly incorporated in our model, although it is known to play a significant role during the electrodeposition[51,52].

To differentiate the Li anode phase and the solid electrolyte phase, we introduce a phase-field variable (ξ), which equals to 1 in Li metal, and 0 in solid electrolyte, and gradually changes from 0 to 1 across the electrode−electrolyte interface (EEI), as illustrated in Fig. 1. Based on these assumptions, the total free energy (*F*) of this half-cell system can be expressed as,

$$F = \int_V [f_{ch}(\xi, c_i) + f_{grad}(\nabla\xi) + f_{elec}(c_i, \varphi) + f_{elas}(\mathbf{F}, \xi)]dV \quad (1)$$

where V is the total volume of the system, f_{ch} , f_{grad} , f_{elec} , f_{elas} are the Helmholtz free energy density, the gradient energy density, the electrostatic energy density, and the elastic energy density, respectively. c_i (i = Li, Li^+ and A^-) denote the local concentrations of the Li metal, the cation, and the anion, and φ represents the local electric potential. The first term (f_{ch}) in Eq. (1) is equal to the summation of a local free energy density (f_0) and an energy of ion mixing (f_{ion}). We will use a double-well function, $f_0(\xi) = W_\xi \xi^2 (1-\xi)^2$ to represent the local free energy density, which yields two local minimum values when $\xi = 0$ and 1, corresponding to the equilibrium electrolyte phase and the Li metal phase. For a dilute electrolyte, the energy of ion mixing can be written as, $f_{ion} = c_0 RT \sum_i c_i^* \ln c_i^*$, where c_i^* is the dimensionless concentration ($c_i^* = c_i / c_0$) and c_0 is the standard bulk concentration (c_0 = 1 mol/L). The gradient energy term in Eq. (1) is represented as $f_{grad}(\nabla\xi) = \frac{\kappa_\xi}{2}(\nabla\xi)^2$ to account for the interfacial energy induced at the Li metal/solid electrolyte interface. The Li dendritic morphology is determined by the anisotropy of the interfacial energy. This can be implemented in the model by tuning the gradient energy coefficient as

$\kappa_\xi = \kappa_0(1+\delta\cos(\omega\theta))$, where κ_0 is a pre-factor term, δ and ω represent the strength and mode of the anisotropy, and θ is the angle between the normal vector of the EEI and the reference axis. The electrostatic energy density in Eq. (1) is written as $f_{elec}(c_i,\varphi) = \rho\varphi = \sum z_i F c_i \varphi$, where ρ , z_i , F represent the local charge density, valence number of different charge species and the Faraday's constant, respectively. Finally, the elastic energy density in Eq. (1) can be represented as $f_{elas} = \frac{1}{2} C_{ijkl}\varepsilon_{ij}^e \varepsilon_{kl}^e$, where C_{ijkl} and ε_{ij}^e represent the elastic stiffness tensor and the elastic strain. Details of the elastic energy density will be discussed in Section 2.2.

The evolution of the phase-field variable (ξ) is modeled by solving the non-linear Landau-Ginzburg-Devonshire (LGD) equation, i.e.,

$$\frac{\partial\xi}{\partial t} = -L_\xi[\frac{\partial f_{ch}}{\partial\xi} - \kappa_\xi\nabla^2\xi - \frac{\partial f_{elas}}{\partial\xi}] - L_\eta h'(\xi)\left\{\exp\left[\frac{\alpha\Delta G(r,t)}{RT}\right] - c_i^* \exp\left[-\frac{\beta\Delta G(r,t)}{RT}\right]\right\} \quad (2)$$

where L_ξ and L_η denote the mobility coefficient for ξ and the reaction rate for the Li^+ deposition reaction ($Li^+ + e^- \leftrightarrow Li$) at the EEI, and $h(\xi) = \xi^3(6\xi^2 - 15\xi + 10)$ is an interpolation function to limit the reduction occuring only at the interface. The evolution rate of ξ is associated with the reduction current expressed by the Butler-Volmer equation (the second term in Eq. (2)). $\Delta G(r,t)$ is the driving force of the electrodeposition reaction and is defined as $\Delta G(r,t) = zF\eta(r,t)$, where $\eta(r,t)$ is the overpotential of the reaction, i.e., the difference between the local electrical potential φ and the standard equilibrium potential φ_0 ($\eta(r,t) = \varphi - \varphi_0$). α and β are the charge transfer coefficients and $\alpha + \beta = 1$.

In this study we assume that Li^+ is the only mobile species of interest driven by

the local electric field. Furthermore, the electrodeposition reaction ($Li^+ + e^- \leftrightarrow Li$) act as a source term for the generation/consumption of Li^+. Thus the evolution of Li^+ concentration (c_{Li^+}) is governed by a Nernst-Planck transport equation,

$$\frac{\partial c_{Li^+}}{\partial t} = \nabla \cdot \left[D_{Li^+}^{eff} \nabla c_{Li^+} + \mu_{Li^+} c_{Li^+} zF \nabla \varphi \right] - K \frac{\partial \xi}{\partial t} \tag{3}$$

where $D_{Li^+}^{eff}$ is the effective diffusivity of Li^+, which is dependent on the Li^+ diffusiviy inside the Li metal ($D_{Li^+}^{m}$) and the solid electrolyte ($D_{Li^+}^{e}$). Thus $D_{Li^+}^{eff}$ can be intepolated as $D_{Li^+}^{eff} = D_{Li^+}^{m} h(\xi) + D_{Li^+}^{e} (1 - h(\xi))$. μ_{Li^+} is the Li^+ mobilty. The last term in Eq. (3) describes the Li^+ concentration variation due to the electrodeposition reaction. It is assumed to be linearly proportional to the evolution rate of ξ ($\partial \xi / \partial t$) via an accumulation constant (K).

The local electrical potential in Eq. (3) is determined by solving the current continuity equation,

$$\nabla \cdot (\sigma^{eff} \nabla \varphi) = R \frac{\partial \xi}{\partial t} \tag{4}$$

Here σ^{eff} is the effective electrical conductivity, which is interpolated as $\sigma^{eff} = \sigma^{m} h(\xi) + \sigma^{e} (1 - h(\xi))$ where σ^{m} and σ^{e} denote the electrical conductivity in the Li metal and the electrolyte. Also, the local charge density change is incorporated by adding a source term related to the electrodeposition reaction ($R \frac{\partial \xi}{\partial t}$) on the right-hand side of Eq. (4), where R is the current constant.

2.2 Solid Mechanics Model

To obtain the elastic energy density (f_{elas}) in the total free of the system (Eq. (1)), the local strain distribution needs to be determined. Based on the continuum

mechanics, the displacement of any point in a continum material can be represented as $\mathbf{u} = \mathbf{x} - \mathbf{X}$, where **u** is a continuous displacement field, **x** is the position of that point at time *t*, and **X** is the position at *t*=0. Thus the total deformation gradient is defined as $\mathbf{F}(\mathbf{X},t) = \nabla_X \mathbf{x}$, where ∇_X represent the gradient operator with respect to **X**. The total deformation gradient (**F**) can further be decomposed into the multiplication of three deformation gradients, i.e.,

$$\mathbf{F} = \mathbf{F_e}\mathbf{F_{inel}}, \quad \mathbf{F_{inel}} = \mathbf{F_0}\mathbf{F_p} \tag{5}$$

where $\mathbf{F_e}$ and $\mathbf{F_{inel}}$ represent the elastic and inelastic deformation gradients, the latter of which can be further decomposed into the deformation gradient ($\mathbf{F_0}$) arising from the Vegard strain due to the local concentration inhomogeneity, and the plastic deformation gradient ($\mathbf{F_p}$).

The local phase transformation strain (ε_{ij}^0) caused by the Li dendrite formation (from Li-ion) and growth can be expressed as $\varepsilon_{ij}^0 = V_{ij}\xi\delta_{ij}$, where V_{ij} is the Vegard strain coefficients which can be obtained from previous literature[53], δ_{ij} is the Kronecker's delta function. Then $\mathbf{F^0}$ can be written as $\mathbf{F_0} = \mathbf{I} + \boldsymbol{\varepsilon}^0$ where **I** is the second-order identity tensor.

The mechanical equilibration of the system occurs at the speed of sound, and is much faster than the Li dendrite growth rate. Therefore, a mechanical equilibrium equation will be solved to estimate the hydrostatic and deviatoric stresses across the entire system, i.e.,

$$\nabla \cdot \mathbf{P}^{\mathbf{T}} + \mathrm{f}_V = 0 \tag{6}$$

where **P** is the first Piola-Kirchhoff stress tensor, f_V is the volume forces and will be

ignored in this work. **P** is related to the second Piola-Kirchhoff stress tensors (**S**) via $\mathbf{P} = \mathbf{FS}$, where **S** is the second Piola-Kirchhoff stress tensor. It is related to the Cauchy stress (**σ**) as,

$$\mathbf{S} = J\mathbf{F}_{\mathbf{inel}}^{-1}\boldsymbol{\sigma}\mathbf{F}_{\mathbf{inel}}^{-\mathbf{T}}; \quad \boldsymbol{\sigma} = \mathbf{C} : \boldsymbol{\varepsilon}^{\mathbf{e}} \tag{7}$$

where J is the Jacobian operator. It converts the infinitesimal element of the volume in the initial configuration into the corresponding fraction of the volume in the intermediate configuration, i.e. $J = \det(\mathbf{F})$. **C** is the elastic constant tensor written as $C_{ijkl} = \frac{E}{2(1+\nu)}\left(\delta_{il}\delta_{jk} + \delta_{ik}\delta_{jl}\right) + \frac{E\nu}{(1+\nu)(1-2\nu)}\delta_{ij}\delta_{kl}$, where E, ν , δ_{ij} denote the elastic modulus of the entire system, the Poisson's ratio, and the Kronecker's delta function. E is dependent on the elastic modulus of the electrode (E^m) and the electrolyte (E^e), i.e., $E = E^m h(\xi) + E^e(1-h(\xi))$. Finally, $\boldsymbol{\varepsilon}^{\mathbf{e}}$ is the elastic strain tensor and is written as $\boldsymbol{\varepsilon}^{\mathbf{e}} = \frac{\mathbf{1}}{\mathbf{2}}(\mathbf{F}_{\mathbf{e}}^{\mathrm{T}}\mathbf{F}_{\mathbf{e}} - \mathbf{I})$ where $\mathbf{F}_{\mathbf{e}} = \mathbf{F}\mathbf{F}_{\mathbf{inel}}^{-1}$.

According to the von Mises stress criterion, plastic deformation happens when the von Mises equivalent stress (σ_v) exceeds the yield strength (σ_y). The von Mises equivalent stress is defined as $\sigma_v = \sqrt{(3/2)\tau_{ij}\tau_{ij}}$, where τ_{ij} is the deviatoric part of Cauchy stress (σ_{ij}), i.e., $\tau_{ij} = \sigma_{ij} - tr(\sigma_{ij})\delta_{ij}/3$. The variation of the yield strength follows the isotropic strain hardening law (Eq. (8)) as,

$$\sigma_y = \sigma_{y_0} + H\varepsilon_{pl}{}^m \tag{8}$$

where σ_{y_0} denotes the initial yield strength, H is the hardening modulus, and m is the hardening exponent. The associated J_2-flow rule is used to obtain the plastic stretch rate as in Eq. (9),

$$\Delta\varepsilon_{ij}^{p} = \frac{3}{2}\frac{\tau_{ij}}{\sigma_{v}}\varepsilon_{eq}^{p} \tag{9}$$

Here $\Delta\varepsilon_{ij}^{p}$ denotes the incremental plastic strain obtained at each load step, ε_{eq}^{p} is the equivalent plastic strain rate and can be calculated as $\varepsilon_{eq}^{p} = \sqrt{\frac{2}{3}\Delta\varepsilon_{ij}^{p}\Delta\varepsilon_{ij}^{p}}$. Then the plastic deformation gradient is written as $\mathbf{F_p} = \mathbf{I} + \boldsymbol{\varepsilon}^{\mathbf{p}}$.

By solving Eq. (6), the total deformation gradient **F** can be obtained from $\mathbf{F} = \mathbf{I} + \nabla\mathbf{u}$, where **u** is the displacement field. Once **F** is obtained, the other mechanical field variables, such as the first and second Piola-Kirchhoff stress tensors (**P** and **S**), and the elastic strain tensor ($\boldsymbol{\varepsilon}^{\mathbf{e}}$) can be defined as a function of **F**. Finally, the elastic energy density can be calculated from $f_{elas} = \frac{1}{2}C_{ijkl}\varepsilon_{ij}^{e}\varepsilon_{kl}^{e}$, in which ε_{ij}^{e} is the component of the elastic strain tensor ($\boldsymbol{\varepsilon}^{\mathbf{e}}$).

2.3 Machine Learning Method

We select four key mechanical properties of the system, i.e., the elastic modulus of the metal electrode (E^{m}) and the solid electrolyte (E^{e}), and the initial yield strength of the metal electrode ($\sigma_{y_0}^{m}$) and the electrolyte ($\sigma_{y_0}^{e}$) as the primary features (or "fingerprints") to identify the potential materials used for the metal anode and the solid electrolyte in the cell. On the other hand, we employ the vertical length of the dendrite structure ($\tilde{L}$) and the area ratio ($\tilde{A}\%$) as the target properties in the machine learning approach.

To obtain the correlations between the four primary features ($E^{m}, E^{e}, \sigma_{y_0}^{m}, \sigma_{y_0}^{e}$) and the two target properties ($\tilde{L}$, $\tilde{A}\%$), a compressed-sensing method named Sure

Independence Screening and Sparsifying Operator (SISSO) is used[54]. The SIS tackles the immense and correlated features, and the SO optimizes the solution from combinations of features. Before building the feature space, the initial yield strengths and elastic modulus are divided by 1MPa and 1GPa respectively to obtain dimensionless results and avoid small number, the target properties, $\tilde{L}$ and $\tilde{A}\%$, are obtained by the dendrite length L and area ratio $A\%$ divided by L_0 and $A_0\%$, respectively, which are the calculated dendrite length and area ratio in the half-cell with PEO electrolyte and lithium metal electrode. To expand the feature space, we assume that the bottom-level feature space (Φ_0) only contains the bottom-level fingerprints, i.e., the four primary features (E^m, E^e, $\sigma^m_{y_0}$, $\sigma^e_{y_0}$). Then the 1st order feature space (Φ_1) will contain complex features (x_j) that are constructed by mathematical operations performed on the bottom-level primary features in Φ_0. We define an operator (H^m) that includes 10 basic mathematical operations, i.e., H^m ={+, -, ×, /, log, ^-1, ^2, ^3, $\sqrt{}$, $\sqrt[3]{}$, | - |}, in which the superscript (m) indicates that only meaningful combinations are considered by grouping the features with the same unit. Following a similar process, feature spaces of higher order (Φ_2, Φ_3) can also be built from the combinations of H^m and the features in the lower-level feature spaces. The number of features in Φ_1, Φ_2, Φ_3 are calculated to be 54, 3183 and 14360474, respectively.

We use Root Mean Square Error (RMSE) as the metrics of this SISSO model,

$$\mathrm{RMSE} = \sqrt{\frac{1}{n}\sum_{i=1}^{n}(y_i - \hat{y}_i)^2} \tag{10}$$

in which n is the number of simulation dataset in the high-throughput database, y_i is

the *i*th value obtained from the phase-field simulation, and $\hat{y}_i$ is the *i*th predicted value from the machine learning model. $\hat{y}_i$ is obtained from the summation of all the features (x_j) in the entire feature space ($\Phi_0 \sim \Phi_3$), weighted by their associated coefficients (θ_j), i.e., $\hat{y}_i = \sum_{j=1}^{m} \theta_j x_j$, which provides a quantitative prediction of the target properties. The regularizer or the sparsifying operator in this model is 'L_0', which is written as,

$$L_0 = \sum_{j=1,\theta_j \neq 0}^{m} \theta_j^0 \tag{11}$$

where θ_j is the *j*th coefficient and *m* is the number of coefficients. Both RMSE and L_0 are minimized during the machine learning process to extract the best *n*D descriptors.

A total of 2337 phase-field simulation results from different combinations of the initial four features are performed to generate a high-throughput database. These datasets are split into the training and test dataset with the ratio of 8:2 after random shuffle. A total of 1870 simulation results are used to train the SISSO model and obtain the corresponding analytical equations, while the remaining 467 simulation results are only used to test and evaluate the trained SISSO model. To benchmark the SISSO model, an additional Deep Neural Network (DNN) model is also implemented. The details of DNN model are provided in the Supplementray Information.

3. Model Implementation

3.1 Parameters used in the model

We first choose Li metal as the anode material, and poly (ethylene oxide) (PEO) as the solid electrolyte in our model system, and employ the phase-field model to simulate a realistic $Li^+ + e^- \leftrightarrow Li$ electrodeposition process in a half-cell system. The entire model is in two dimension (2D) and is solved by the finite element method on the platform of COMSOL Multiphysics 5.4. The total system size is $900\times900\mu m^2$ with an adaptive mesh size from 1.8×10^{-2} to 9μm, defined by the COMSOL default extremely fine mode. To keep convergence and avoid numerical errors, the nonlinear method of the time-dependent solver is set to be Automatic highly nonlinear (Newton) instead of Constant (Newton) with a maximum number of iterations as 30. The Li^+ concentration (c_{Li^+}) is normalized by a bulk concentration c_0 = 1mol/L, i.e., $\tilde{c}_{Li^+} = c_{Li^+} / c_0$. Similarly, the other parameters in the electrochemical part are normalized by a characteristic energy density E_0=1.5×10^6 J/m^3, a characteristic length l_0 =100μm, a characteristic time step t_0 =400s, and their combinations. For the mechanical part, all the parameters are normalized by a characteristic strength $S_0 = 1.0$GPa . The charge transfer coefficients are set to be $\alpha = \beta = 0.5$. The temperatures in all simulations are set to be 298K. All parameters used in this model and their normalized method are listed in Table 1.

Table 1 Parameters used in the phase-field model

Parameters	Symbols	Real Values	Symbols	Normalized Values	References
Interfacial mobility	L_ξ	5.6×10^{-6} m^3/(J×s)	$\tilde{L}_\xi = L_\xi \times (E_0 \times \Delta t_0)$	3333	[45,55]

Reaction constant	L_η	1.39×10^{-6} $m^3/(J\times s)$	$\tilde{L}_\eta = L_\eta \times (E_0 \times \Delta t_0)$	833.25	[45,55]
Gradient energy coeff. 1	κ_0	1.5×10^{-4} J/m	$\tilde{\kappa}_0 = \kappa_0 / (E_0 \times l_0^2)$	0.01	[45,55]
Li^+ diffusivity in the electrode	D^m	2.5×10^{-14} m^2/s	$\tilde{D}^m = D^m / (l_0^2 / \Delta t_0)$	10^{-3}	[45,55]
Li^+ diffusivity in the electrolyte	D^e	2.5×10^{-11} m^2/s	$\tilde{D}^e = D^e / (l_0^2 / \Delta t_0)$	1.0	[56]
Electric conductivity in the electrode	σ^m	1.0×10^6 S/m	$\tilde{\sigma}^m = \sigma^m / (\frac{l_0^2}{\Delta t_0} \bullet \frac{c_0 F^2}{RT})$	10^7	[45,55]
Electric conductivity in the electrolyte	σ^e	1.0×10^{-1} S/m	$\tilde{\sigma}^e = \sigma^e / (\frac{l_0^2}{\Delta t_0} \bullet \frac{c_0 F^2}{RT})$	1.0	[37]
elastic modulus of the electrode	E^m	4.9GPa	$\tilde{E}^m = E^m / 1GPa$	4.9	[17]
elastic modulus of the polymer electrolyte	E^e	0.3GPa	$\tilde{E}^e = E^e / 1GPa$	0.3	[17]
Initial yield strength of the electrode	$\sigma_{y_0}^m$	0.4MPa	$\tilde{\sigma}_{y_0}^m = \sigma_{y_0}^m / 1GPa$	4×10^{-4}	[27,57]
Initial yield strength of the polymer	$\sigma_{y_0}^e$	0.77MPa	$\tilde{\sigma}_{y_0}^e = \sigma_{y_0}^e / 1GPa$	7.7×10^{-4}	[58, 59]

electrolyte					
Partial molar volume of the electrode	V_m	1.3×10^{-5} m^3/mol	$\tilde{V}_m = V_m \times c_0 / 10^3$	1.3×10^{-5}	[17]
Partial molar volume of polymer electrolyte	V_e	1.674×10^{-4} m^3/mol	$\tilde{V}_e = V_e \times c_0 / 10^3$	1.674×10^{-4}	[17]
Lithium transference number	t_{Li^+}	0.3		0.3	[17,60]
Strength coefficient of the electrode	H_m	1.9MPa	$\tilde{H}_m = H_m / 1GPa$	1.9×10^{-3}	[27, 57]
Strength coefficient of the electrolyte	H_e	3.5MPa	$\tilde{H}_e = H_e / 1GPa$	3.5×10^{-3}	[58,59]
Hardening exponent of the electrode	m_m	0.4		0.4	[27,57]
Hardening exponent of the polymer electrolyte	m_e	0.4		0.4	[58,59]
Poisson's ratio	v	0.36		0.36	[53]
Eigenvalues of the strain tensor	V_1	-0.866×10^{-3}		-0.866×10^{-3}	[61]
	V_2	-0.773×10^{-3}		-0.773×10^{-3}	
	V_3	-0.529×10^{-3}		-0.529×10^{-3}	

Charge transfer coefficients	α, β	0.5		0.5	[45,55]
Accumulation constant	K	1.8mol/L	$\tilde{K} = K / c_0$	1.8	[45,55]
Strength of anisotropy	Δ	0.02		0.02	[45,55]
Mode of anisotropy	Ω	4.0		4.0	[45,55]
Current constant	R	1.5×10^5J/m^3	$\tilde{R} = R / E_0$	0.1	[45,55]

3.2 Boundary Conditions

For the electrochemical part, zero-flux boundary conditions are applied to the four boundaries for the order parameter ξ (Eq. (2)). When solving the Li^+ transport and the electrical potential distribution (Eq. (3) and (4)), Dirichlet boundary conditions are applied at the right side and left/right sides of the system, respectively, while zero-flux boundary conditions are used for the other sides. For the mechanical part, periodic boundary conditions are applied to the top and bottom sides of the system, while fixed constraint boundary conditions are used for the other sides. All the boundary conditions above are shown schematically in Fig. 1a. The 2D approximation is made such that the out-of-plane strain vanishes[62].

3.3 Initial Conditions

All the simulations in this study start with an initial state which consists of a

solid electrolyte phase of high Li^+ concentration, and a small protrude of Li metal at the electrode surface of low Li^+ concentration to mimic a single broken point on the SEI layer. The electrical potential is fixed at the electrode (φ=-0.35V) and the right side of the simulation system (φ=0V) which is indicated in Fig. 1a, and is linearly extrapolated in between in the initial state.

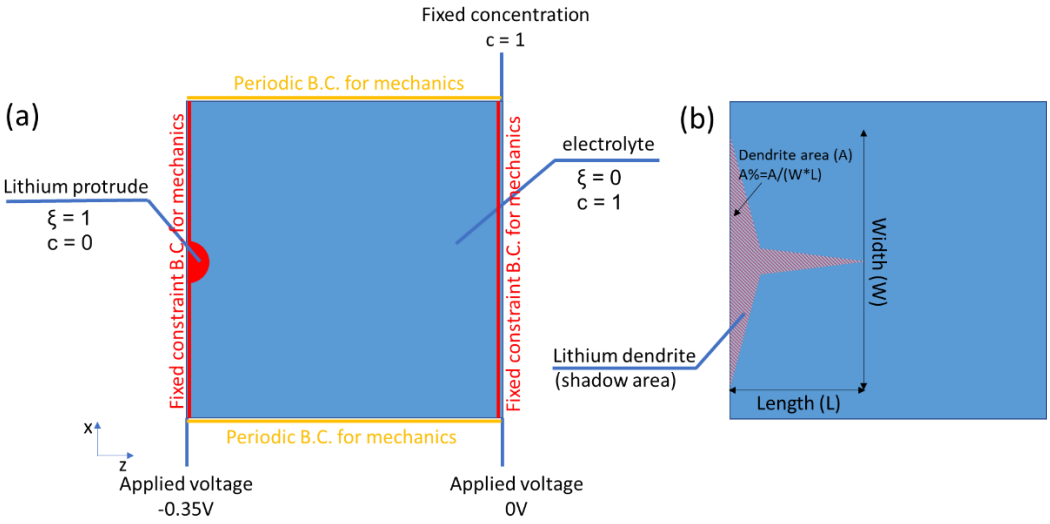

Figure 1 (a) Schematic diagram of boundary conditions, initial state of the system and (b) definitions of dendrite length (L), width (W) and area ratio (A%).

4. Results and Discussions

4.1 Li dendrite growth in PEO electrolyte

We start with the case when the Li dendrite grows inside the PEO polymer electrolyte. The parameters used in the simulation are listed in Table 1, and initial and boundary conditions are shown in Fig. 1a. Fig. 2 shows the temporal evolutions of the Li dendrite morphology (ξ), lithium-ion concentration (c_{Li^+}), electrical field component distribution (E_z), equivalent plastic strain (ε_{eq}^p), and local hydrostatic strain (ε_h), respectively. First, a lithium protrude is introduced at the center of the Li anode surface

to mimic the initial nucleation of Li dendrite (Fig. 2(a)). Under an applied bias of -0.35V, Li ions in the electrolyte migrate towards the protrude where local electric field is enhanced, and are subsequently reduced to Li metal by the electrons in the electrode. This results in a progressive growth of the Li protrude into a dendrite morphology due to the inhomogeneous interfacial energy (Fig. 2(b)-(d)). The simulated Li dendrite agrees well with the experimentally observed dendritic morphology (Fig. S1). Fig. 2(e) illustrates the 2D plots of the Li-ion concentration (c_{Li^+}) and local electric field component (E_z) along the vertical (z) direction at t=500s, as well as the 1D temporal evolutions of c_{Li^+} and E_z along the directions as indicated by the arrows in the 2D inset plots. It is seen that c_{Li^+} remains almost constant in the electrolyte (~1.0 mol/L) and Li anode (~0.0 mol/L), and decreases across the Li dendrite/electrolyte interface. This induces a large Li-ion concentration gradient at the electrode-electrolyte interface, which acts an electrochemical driving force (based on the Bulter-Volmer kinetics in Eq. 2) to promote the Li dendrite growth. Furthermore, the local electric field (E_z) is almost constant inside the electrolyte and the Li anode, and the maximum local field (absolute value) is seen at the tip of the Li dendrite (2D plot in Fig. 2e). This maximum local electric field (absolute value) at the dendrite tip increases over time (1D evolution plot in Fig. 2e), indicating that the Li dendrite growth is a self-accelerating process, which agrees with previous reports[63]. The 2D equivalent plastic strain (ε_{eq}^{p}) and the value of hydrostatic strain $\varepsilon_h = \frac{1}{3}(\varepsilon_{11}^{e} + \varepsilon_{22}^{e} + \varepsilon_{33}^{e})$ at the final state (t=500s), as well as the 1D temporal evolutions of ε_{eq}^{p} and ε_h (along directions indicated by the arrows in the 2D inset plots) are illustrated in Fig. 2(f)-(g). It is seen that both ε_{eq}^{p} and ε_h remain

high in the Li metal, and are negligible inside the solid electrolyte. ε_h reaches the maximum value (~ -7×10^{-4}) in the core of the Li dendrite, and gradually decreases towards the tip of the Li dendrite (~ -4×10^{-4}). Similarly, the equivalent plastic strain (ε_{eq}^{p}) mainly exists inside the lithium metal, and its magnitude decrease from the Li dendrite core to the tip, which agrees with the hydrostatic strain distribution. It is noteworthy that the maximum ε_{eq}^{p} can reach up to 5×10^{-3}, almost one order of magnitude higher than the hydrostatic strain. This indicates that a significant plastic deformation could occur inside the Li metal, due to its low initial yield strength.

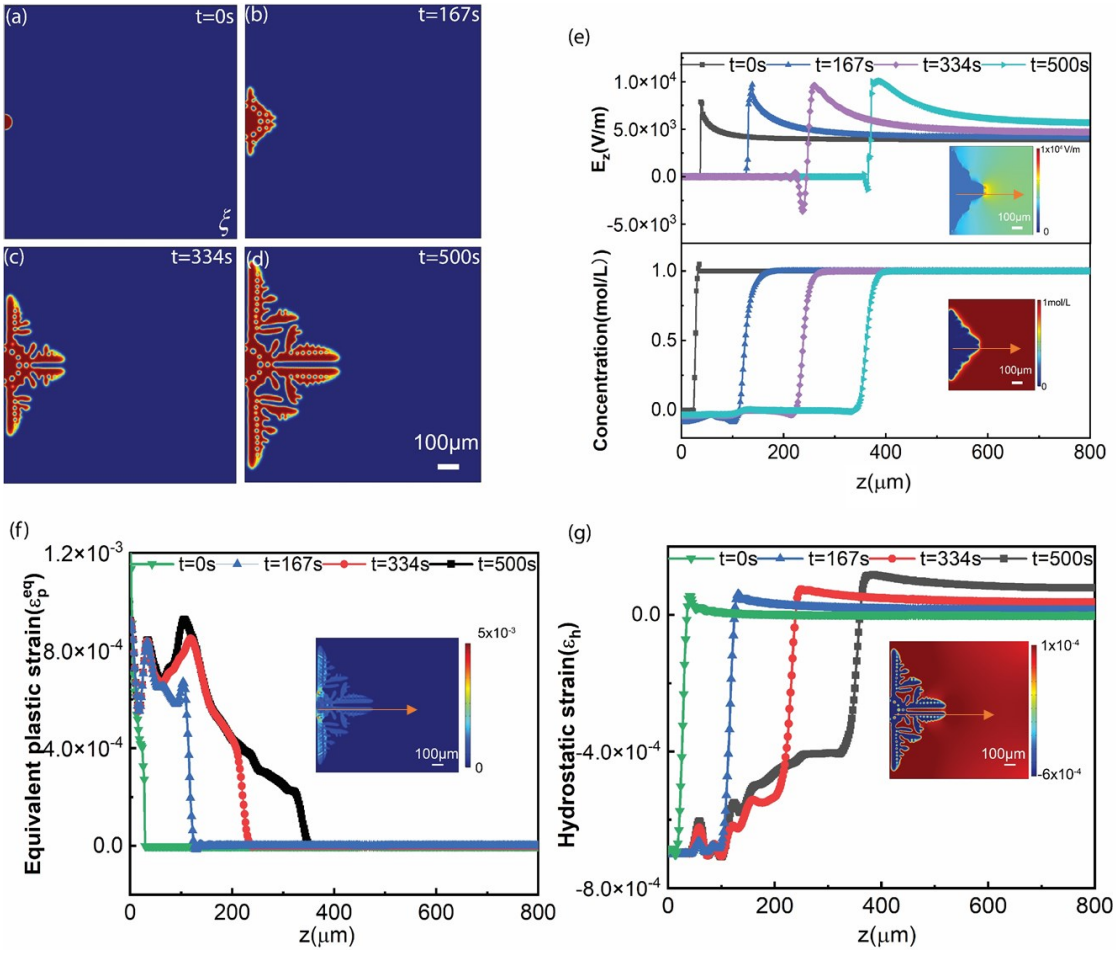

Figure 2 Phase-field simulation results of Li dendrite growth in PEO. (a)-(d) the temporal evolution of dendrite morphology from 0s to 500s, (e) Evolutions of Li-ion concentration (c_{Li^+}) (lower) and the

electrical field component (E_z) (upper) along the arrow segment indicated in the inset figures, (f) equivalent plastic (ε_{eq}^{p}) and (g) hydrostatic strain (ε_h) evolution with time along the arrow segment indicated in the inset figures.

4.2 Effect of elastic modulus of solid electrolyte on the dendrite growth

To further understand the mechanical properties of the solid electrolyte on the Li anode stability, we simulate the Li dendrite growth behavior in solid electrolytes of different elastic moduli (E^e's) that range from 5.0 to 50GPa. While the yield strength of the solid electrolyte ($\sigma_{y_0}^{e}$) usually increases with increasing E^e, here we assume that $\sigma_{y_0}^{e}$ is fixed to be 7.7MPa in all cases to better understand the pure elastic effect of the electrolyte. The elastic modulus (E^m) and the yield strength ($\sigma_{y_0}^{m}$) of the Li metal electrode are fixed to be 5GPa and 0.4MPa, respectively. Fig. 3(a)-(d) illustrate the final morphology of the Li dendrites after evolving for 500s in solid electrolyte of different elastic moduli (E^e's). It is clearly seen that when E^e increases, the dendrite growth is inhibited in the vertical direction (along z). Furthermore, the growth of side branches from the primary arm of Li dendrite is also inhibited when E^e increases. This trend agrees well with our previous work and the well-recognized theory[17,48]. To further understand this effect, we compare the elastic driving force at the electrode-electrolyte interface, calculated as $\frac{-\partial f_{elas}}{\partial \xi}$ (Fig. 3(e)-(h)), with the sum of the remaining driving force $\frac{-\partial (f_{ch}+f_{grad}+f_{elec})}{\partial \xi}$ (Fig. S2 (i)-(l)). The sum of the remaining driving force is found to be positive along the Li/electrolyte interface, indicating that the

electrochemical reaction as described by the Butler−Volmer kinetics promotes the Li dendrite growth. Furthermore, the remaining driving forces are almost constant (~6×10^{-2} J/m^3) in all cases, due to the fact that the gradients of the Li^+ concentration and the electrical potential are less dependent on the elastic modulus of the electrolyte (Fig. S2). In contrast, the elastic driving force at the interface varies from -3 to -12 (10^{-3} J/m^3) when E^e changes from 5.0 to 50GPa (Fig. 3 (e)-(h)). Since a negative elastic driving force favors the ξ evolution from 1.0 to 0.0, i.e., the Li dendrite growth is inhibited, thus a more negative elastic driving force due to a larger elastic modulus of the electrolyte can better offset the positive remaining driving force, and finally leads to a better Li dendrite inhibition effect. The von Mises stress distributions (Fig. 3 (i)-(l)) indicate that the plastic yielding could occur based on the overall level of deviatoric stress τ_{ij}. It is seen that larger deviatoric stress (light blue region) is mainly distributed at the tips of the dendrite, and in the spacings between neighboring Li dendrite branches. The magnitude of the von Mises stress increases with increasing E^e.

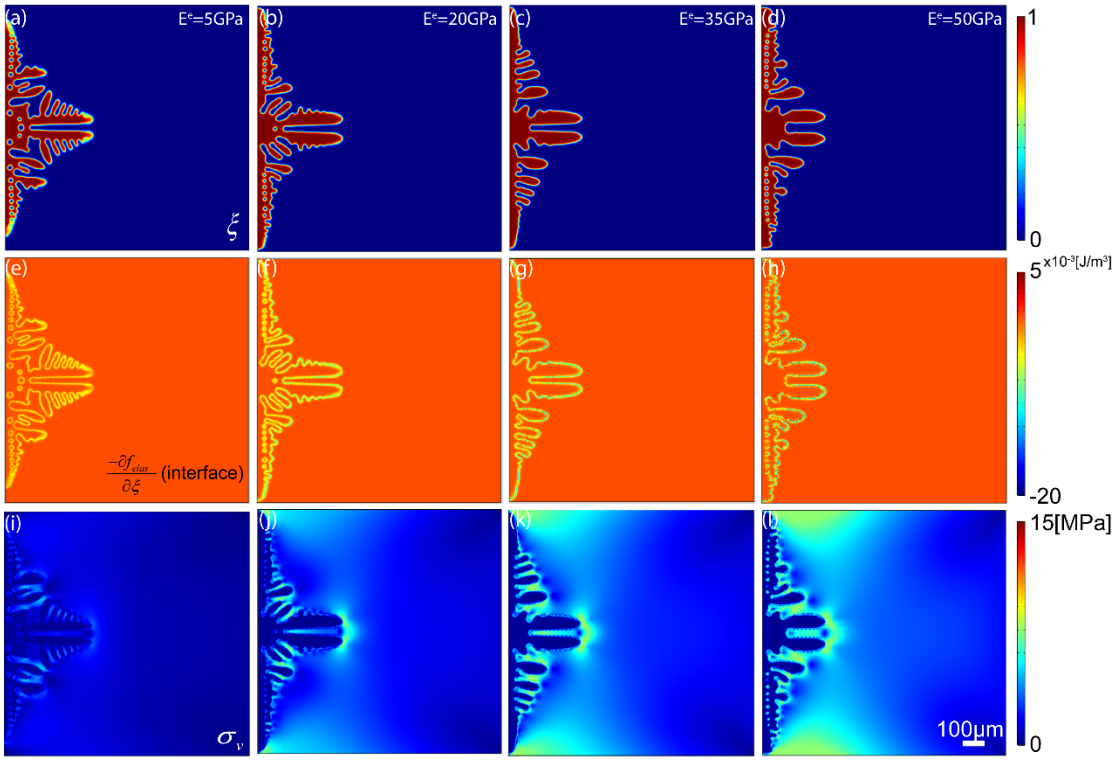

Figure 3 Dendrite morphology (a)-(d), the corresponding elastic driving force (e)-(h) and the von Mises stress distribution (i)-(l) from the phase-field simulation results after 500s evolution in solid electrolytes of different elastic moduli (E^e). The elastic moduli of the electrolyte are (a)5GPa; (b) 20GPa; (c) 35GPa; (d) 50GPa. The yield strength of the electrolyte ($\sigma_{y_0}^e$) is fixed to be 7.7MPa.

4.3 Effect of yield strength of solid electrolyte on the dendrite growth

We further study the effect of yield strength of the solid electrolyte ($\sigma_{y_0}^e$) on the Li dendrite growth. Here the magnitude of $\sigma_{y_0}^e$ is selected to be from 0.77 to 77MPa, while the elastic modulus of the electrolyte is fixed to be 35GPa. The elastic modulus and the yield strength of the metal electrode are chosen to be the same as in section 4.2. Fig. 4(a)-(c) illustrates the final morphology of Li dendrite after 500s evolution with $\sigma_{y_0}^e$'s of solid electrolyte. It is seen that the Li dendrite growth is effectively inhibited

when $\sigma_{y_0}^e$ increases from 0.77MPa to 7.7MPa (Fig. 4(a)-(b)), resulting in a shorter length of primary Li dendrite arms, and the reduced side branch growth from the primary arm. This is because of a more negative elastic driving force at the electrode-electrolyte interface, which mainly inhibits the Li dendrite growth (Fig. 4(d)-(e)). However, when $\sigma_{y_0}^e$ further increases from 7.7MPa to 77MPa, the vertical length of the primary arms of the Li dendrite remains almost the same, although secondary arms are further inhibited (Fig. 4(b)-(c)), indicating that the inhibition effect is less significant when $\sigma_{y_0}^e$ is abovel 7.7MPa (Fig. 4(e)-(f)). To further understand this trend, we compare the distributions of the von Mises stress (σ_v) under different $\sigma_{y_0}^e$'s (Fig. 4(g)-(i)). The maximum deviatoric stress of the von Mises stress (σ_v) is found to be inside the electrolyte and close to the electrode-electrolyte interface. Its value is well below the yield strength of the electrolyte when $\sigma_{y_0}^e$ = 0.77MPa (Fig. 4g). When $\sigma_{y_0}^e$ increases from 0.77MPa to 7.7MPa, the maximum σ_v also increases accordingly (Fig. 4h), which further inhibits the Li dendrite growth (Fig. 4b). However, when σ_v reaches its maximum value under given E^e (~10 MPa for E^e =35GPa in this case), further increase of $\sigma_{y_0}^e$ (from 7.7MPa to 77MPa) can no longer enhance the deviatoric stress to further inhibit the Li dendrite growth (Fig. 4i). This is further illustrated in a schematic stress-strain curve of the solid electrolyte with different $\sigma_{y_0}^e$'s (Fig. 4j). Under a smaller $\sigma_{y_0}^e$ (case 1), the maximum deviatoric stress (σ_v^1) with a given deformation strain is mainly limited by the initial yield strength of the electrolyte ($\sigma_{y_0}^e$). In this case, the increase of $\sigma_{y_0}^e$ (from case 1 to 2) gives rise to a larger deviatoric stress (σ_v^2) to effectively suppress the Li dendrite growth. However, when $\sigma_{y_0}^e$ exceeds the

maximum limit of the deviatoric stress that could be induced under given elastic modulus, further increase of $\sigma_{y_0}^e$ (case 2 to 3) could no longer enhance σ_v^2, and is less effective in the Li dendrite suppression. In this case, the Li dendrite can only be inhibited by further increasing the elastic modulus of the solid electrolyte (case 4 ~ 6 in Fig. 4k). Therefore, effective inhibition of the Li dendrite growth requires both a large elastic modulus that is able to induce large deviatoric stress, and a corresponding yield strength that allows the deviatoric stress to reach its maximum value.

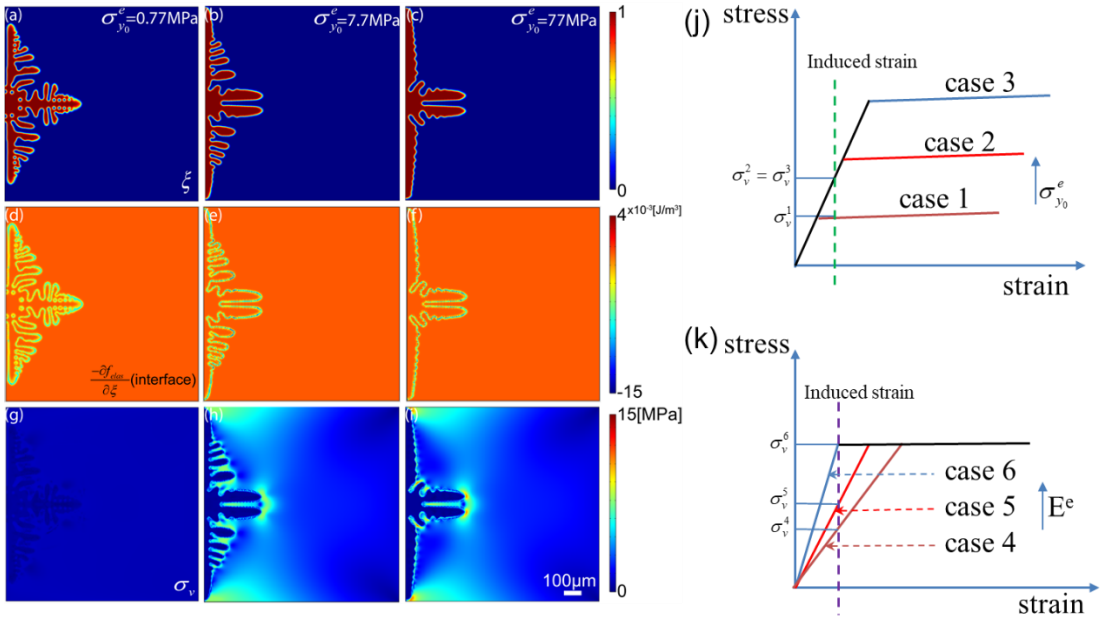

Figure 4 Dendrite morphology(a)-(c), elastic driving force (d)-(f) and corresponding von Mises stress distribution (g)-(i) from the phase-field modeling after 500s evolution in the polymer electrolyte of different yield strength ($\sigma_{y_0}^e$): (a) 0.77MPa; (b) 7.7MPa; (c) 77MPa. The elastic modulus of electrolyte (E^e) is fixed at 35GPa. (j)-(k) Schematic diagram of the von Mise stress change when the yield strength increases at fixed elastic modulus (j), and when the elastic modulus increases at fixed yield strength (k), based on the assumption of fixed induced strain.

4.4 Effect of yield strength of metal electrode on the dendrite growth

As the yield strength of Li metal may vary by several orders of magnitude (10^{-1} ~10^{1}MPa) which is dependent on the creep behavior, stretch rate and size effect[24–26,29], here we continue to investigate the effect of the yield strength of metal electrode ($\sigma_{y_0}^m$) on the metal dendrite growth. Fig. 5(a)-(c) illustrates the final morphology of the metal dendrite after 500s evolutions when $\sigma_{y_0}^m$ varies from 0.4 to 40MPa. The elastic modulus of the Li metal electrode and the solid electrolyte, and the yield strength of the electrolyte are set to be 5GPa, 35GPa, and 0.77MPa, respectively. From Fig. 5(a)-(c), it is seen that the Li dendrite growth is better inhibited when $\sigma_{y_0}^m$ increases, similar to the inhibition effect by the solid electrolyte (Fig. 4(a)-(c)). However, the major difference is that here both the vertical (along z) and lateral (along x) growth of the dendrite structure are inhibited when $\sigma_{y_0}^m$ increases, while in Fig. 4(a)-(c) only the vertical growth of the dendrite structure is suppressed, and its lateral growth is slightly promoted when σ_{y0}^e increases. The elastic driving forces ($-\partial f_{elas} / \partial \xi$) under different $\sigma_{y_0}^m$ s are further compared in Fig. 5(d)-(f). It is seen that their values are almost the same along the electrode-electrolyte interface for all cases. However, from the von Mises stress distribution as shown in Fig. 5(g)-(i), the high deviatoric stress is mainly seen inside the metal electrode, which increases with increasing $\sigma_{y_0}^m$. This is significantly different from the deviatoric stress distribution and magnitude under different $\sigma_{y_0}^e$'s, in which maximum deviatoric stress are seen inside the electrolyte and along the electrode-electrolyte interface (Fig. 4(g)-(i)). Therefore, the deviatoric stress might be responsible for the inhibition of Li dendrite growth. Our simulation results are

different from previous studies by Barai *et. al.* [40]. In their work, the effective suppression of the dendritic protrusion occurs when the lithium electrode undergoes plastic deformation, and the polymer electrolyte is only elastically deformed. However, based on our simulation results, the Li dendrite can be better inhibited when both lithium electrode and polymer electrolyte are in the elastic deformation region. This is probably because a high Li metal yield strength enables the electrode to endure higher stress induced by the mechanical suppression before plastic deformation occurs. It is noteworthy that here we only show one scenario of the effect of $\sigma_{y_0}^m$ on the metal dendrite growth (E^m =5GPa , E^e =35GPa, $\sigma_{y_0}^e$ =0.77MPa). In fact, under different combinations of the E^m , E^e , and $\sigma_{y_0}^e$, the trend of the Li dendrite growth with increasing $\sigma_{y_0}^m$ may not be monotonous, which makes the overall trend more complicated (See Fig. S3 and discussions in the SI). Therefore, a more comprehensive analysis of the effect of yield strength of the metal electrode is needed.

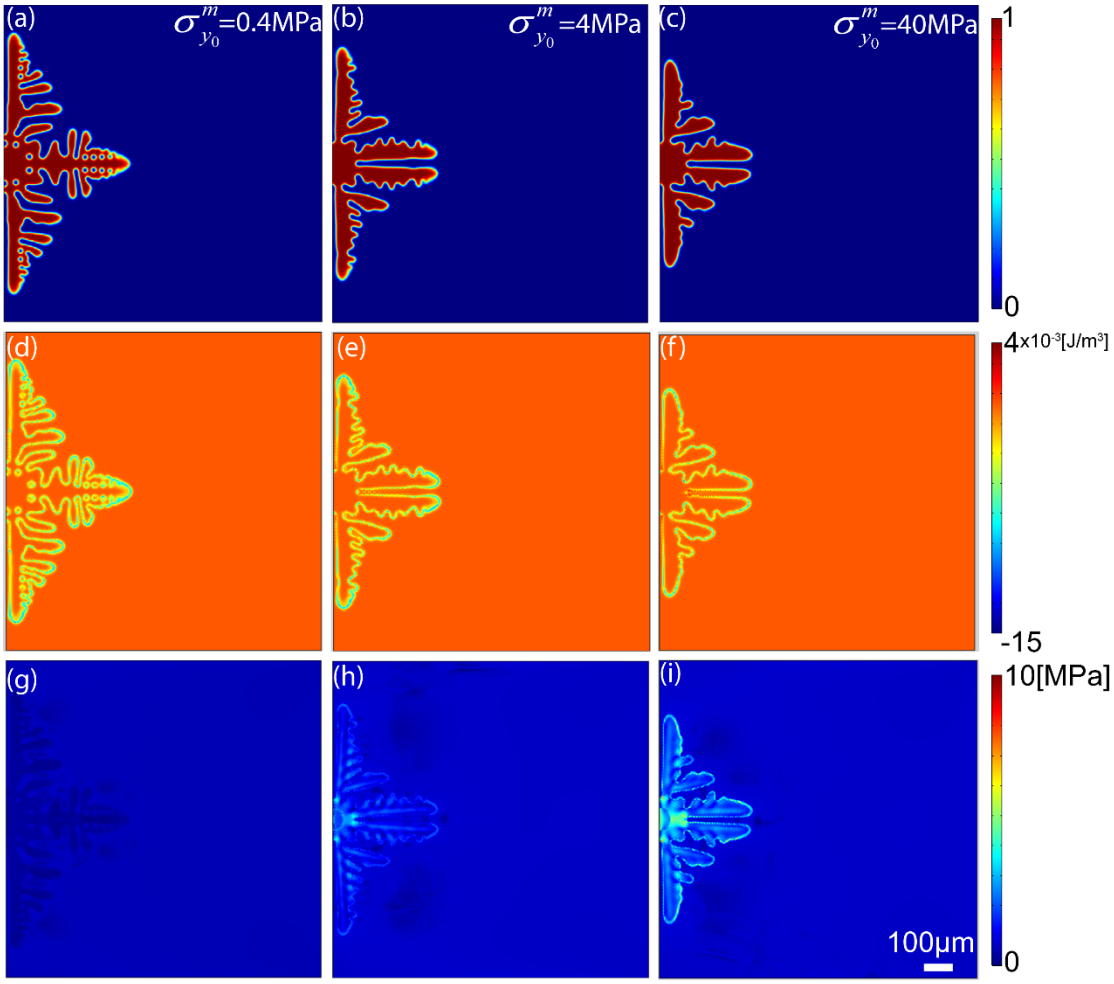

Figure 5 Dendrite morphology(a)-(c), the corresponding elastic driving force(d)-(f) and the von Mises stress distribution (g)-(i) from the phase-field model after 500s evolution under the Li metal of different initial yield strength ($\sigma_{y_0}^m$). The initial yield strengths of metal are as indicated in the first row of figure which are: 0.4MPa (a)(d)(g); 4MPa (b)(e)(h) and 40MPa (c)(f)(i). The elastic modulus of the electrolyte is 35GPa.

4.5 High-throughput phase-field simulations

To investigate the overall trend of the inhibitory effect from the three mechanical properties ($\sigma_{y_0}^m$, $\sigma_{y_0}^e$ and E^e), we perform the high-throughput phase-field simulations by varying the magnitudes of the above three mechanical properties, and

calculating the corresponding dendrite length (L) and the area ratio (A%). Here L measures the growth rate of the Li dendrite. It is directly obtained from the simulated dendrite morphology. A% illustrates the side growth of the dendrite, which is calculated from the dendrite area (A) divided by the product of dendrite length (L) and width (W), i.e., $A\% = A/(W\times L)$, as illustrated in Fig. 1b. Thus, a low value of A% indicates the limited side growth under the similar dendrite main growth (L) along the vertical direction. The ranges of $\sigma_{y_0}^m$, $\sigma_{y_0}^e$ and E^e are chosen to be 0.4-20MPa, 1-45MPa and 0.3-50GPa, respectively, which include most of the polymer electrolytes, and cover the variation of $\sigma_{y_0}^m$ caused by the creep, stretch rate, and size effect. The high-throughput calculation results are shown in Fig. 6(a) and (b). From Fig. 6(a), it is seen that the Li dendrite lengths after 500s evolution vary from 170μm to 447μm. As a general trend, under a combination of higher $\sigma_{y_0}^e$ and higher E^e, the Li dendrite length is minimized among all-range of $\sigma_{y_0}^m$. In contrast, increasing the $\sigma_{y_0}^m$ only helps to mitigate the dendrite growth at a higher E^e but lower $\sigma_{y_0}^e$. On the other hand, the plot of area ratio (A%) (Fig. 6b) indicates that the combination of higher $\sigma_{y_0}^e$ and E^e also contributes to the inhibition of the dendrite side growth, while the influence of $\sigma_{y_0}^m$ is not obvious compared to the other two parameters.

To clearly identify the trends from the 3D database, the 2D maps of the dendrite length and area ratios are plotted as a function of any two out of the three parameters. Fig. 6(c) shows the Li dendrite length as a function of E^e and $\sigma_{y_0}^e$ at a fixed $\sigma_{y_0}^m$ of 0.4MPa. A region of low dendrite length is clearly seen at the upper-right corner of Fig. 6c (a red circle), which corresponds to certain solid electrolyte of higher elastic

modulus and yield strength. In contrast, at a fixed E^e = 20GPa (Fig. 6(d)) or a fixed $\sigma_{y_0}^e$ = 2MPa (Fig. 6(e)), the region corresponding to the lowest dendrite length in the 2D maps is scattered. The trend in the area ratio (Fig. 6(f-h)) is also similar to the dendrite length, i.e., increasing E^e and $\sigma_{y_0}^e$ help inhibit the dendrite side growth. Based on our simulation results, the solid electrolyte with both higher E^e and $\sigma_{y_0}^e$ is most effective in the dendrite inhibition and thus could potentially increase the life cycles of the cells under similar testing conditions. This agrees with a recent report on the trend of the cycle life of various solid-electrolyte battery systems[37], in which different solid electrolytes, such as PEO [17], lithium sulfide ($Li_2S–P_2S_5–MS_x$)[64], and thin film LiPON[65] with increasing elastic moduli from 0.3GPa to 77GPa, also exhibit increasing life cycles from 400 to 10,000, which are generally considered to be due to a stable Li plating/stripping during the charge/discharge cycling. However, if only the condition of higher E^e is met, tuning the yield strength of the metal ($\sigma_{y_0}^m$) can also help reduce the dendrite growth. Our simulation results agree with previous literature that mechanically stiff solid-state electrolyte (high E^e & $\sigma_{y_0}^e$) are more effective in preventing the dendrite propagation[17]. Meanwhile, the initial yield strength of Li metal is related its creep behavior, which plays a critical role in the mechanical suppression of dendrite growth. On the one hand, when E^e is high, the induced mechanical stack stress can suppress void formation in the metal through beneficial creep[66–69]. On the other hand, the detrimental creep will, in extreme cases, cause the lithium extrusion around the electrolyte and eventually cause short circuit[30]. The complexity in the creep behavior of Li metal may be the reason for different trends of the inhibitory effects of

Li dendrite from the yield strength of metal electrodes.

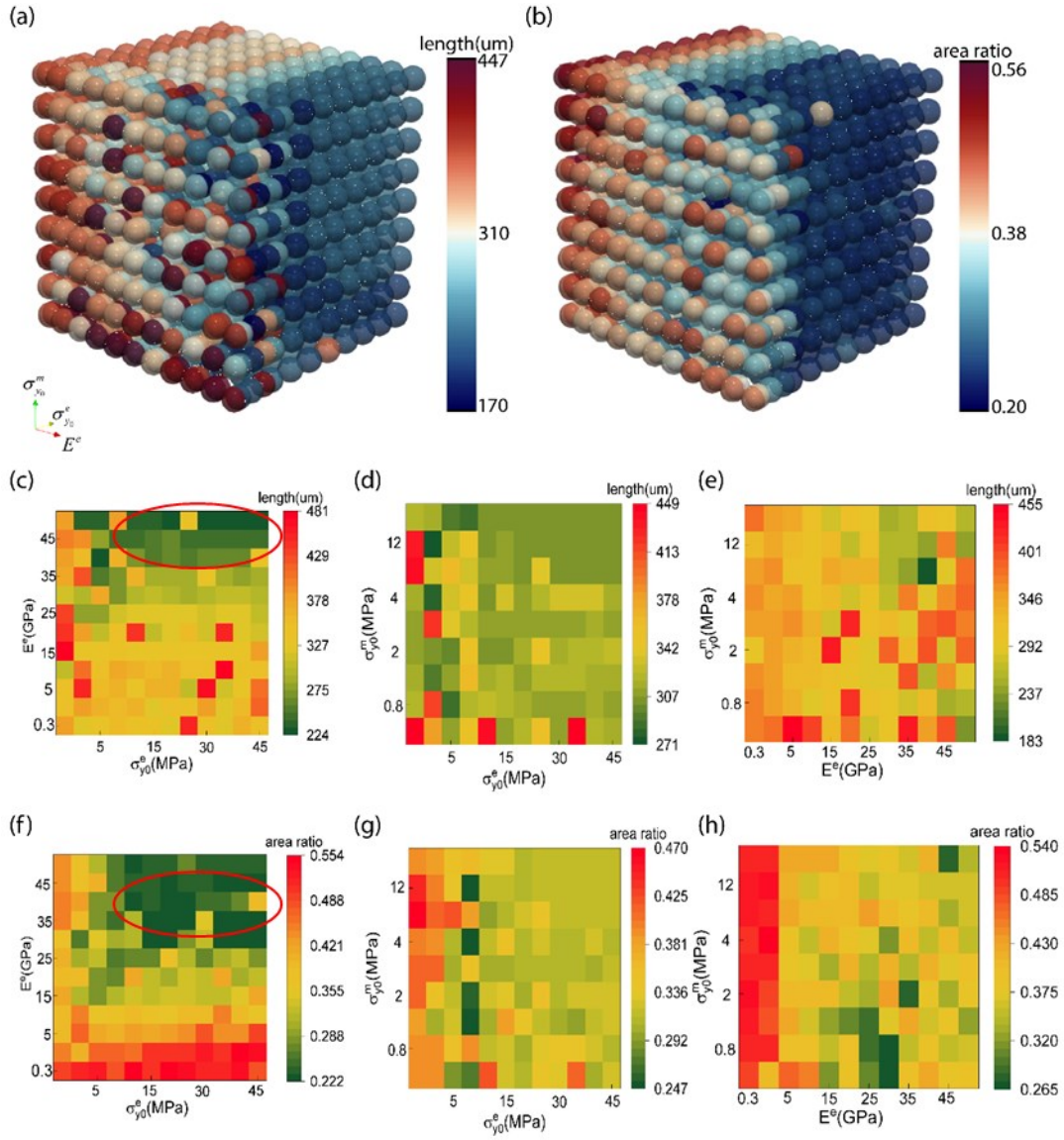

Figure 6 High-throughput phase-field simulation results. (a) the length and (b) the area ratio of the dendrite growth by parameterizing the three mechanical properties, i.e., the initial yield strength of metal ($\sigma_{y_0}^m$) and electrolyte ($\sigma_{y_0}^e$) and elastic modulus of electrolyte (E^e). 2D mapped dendrite length (c)-(e) and area ratio (f)-(h) as cross sections of the 3D results by fixing one of the three properties ((c)&(f) $\sigma_{y_0}^m$ is fixed at 0.4MPa, (d)&(g) E^e at 20GPa, (e)&(h) $\sigma_{y_0}^e$ at 2MPa). The elastic modulus of lithium metal is set to be 5GPa.

4.6 Machine Learning Model

Based on the high-throughput calculation results, we develop a machine-learning model to explore the correlation between the mechanical properties (elastic moduli and initial yield strength) and the dendrite morphology (length and area ratio). In addition to the three parameters ($\sigma_{y_0}^m$, $\sigma_{y_0}^e$, E^e) from the high-throughput simulations, elastic modulus of the metal electrode (E^m) is also included, so that the model can also provide some guidance to other battery systems. It is noteworthy that the dendrite length and area ratio are dependent on many factors, such as the initial protuberant morphology, interfacial roughness, internal temperature in the cell, as well as the external conditions such as the magnitude and duration of the applied voltage, current density, etc[45]. Here we develop a machine learning model not to quantitatively predict the dendrite morphology, but to elucidate the relative importance of the mechanical properties of the electrode and electrolyte in the dendrite growth behavior. A recently developed Sure Independence Screening and Sparsity Operator (SISSO)[54] machine learning approach is employed to train the database and predict the dendrite length as well as area ratio. SISSO not only allow us to screen the combinations of input parameters with physical meanings to build the huge feature space using the sure independence screening (SIS) but also filter out the correlated features with sparsity operator (SO). The root mean squared error (RMSE) is used as the metrics to construct the features in descriptors. After training the datasets, we choose the 3D-descriptor as the predictive expression of relative dendrite length ($\tilde{L}$) with RMSE = 0.163 and relative area ratio ($\tilde{A}\%$) with RMSE = 0.109, as shown in Eqs. 12, 13.

$$\begin{aligned}\tilde{L} = &-1.25\times10^{-2}\times\left(\frac{\tilde{E}^e}{\sqrt{\tilde{E}^m}}+\log\tilde{\sigma}_{y_0}^m\sqrt{\tilde{E}^m}\right)\\ &+5.30\times10^{-2}\times\left\|\log\tilde{E}^e-\log\tilde{\sigma}_{y_0}^e\right|-\left|\log\tilde{E}^m-\log\tilde{\sigma}_{y_0}^m\right\|+0.97\end{aligned} \tag{12}$$

$$\begin{aligned}\tilde{A}\% = &-0.41\times(\tilde{E}^e-\tilde{\sigma}_{y_0}^m)\frac{\sqrt[3]{\tilde{\sigma}_{y_0}^e}}{\tilde{E}^e+\tilde{\sigma}_{y_0}^e}\\ &+8.4\times10^{-5}\times(\tilde{E}^m-\left|\tilde{E}^e-\tilde{\sigma}_{y_0}^m\right|)(\tilde{\sigma}_{y_0}^e+\tilde{\sigma}_{y_0}^m-\left|\tilde{E}^e-\tilde{E}^m\right|)+1.296\end{aligned} \tag{13}$$

where $\tilde{E}^e$, $\tilde{E}^m$ are the reduced values of E^e , E^m , which are normalized by 1GPa,

while $\tilde{\sigma}_{y_0}^{e}$, $\tilde{\sigma}_{y_0}^{m}$ represent the reduced values of $\sigma_{y_0}^{e}$, $\sigma_{y_0}^{m}$, which are normalized by 1MPa, $\tilde{L}$ and $\tilde{A}\%$ are obtained via dividing L and A% by L_0 and A_0%, the latter of which are calculated from the phase-field simulation using PEO solid electrolyte and Li metal electrode.

When the elastic modulus of the metal is fixed (E^m=5GPa), the first term on the right-hand side of Eq. 12 indicates that when E^e or $\sigma_{y_0}^{m}$ increases, the dendrite length will decrease (due to a negative coefficient of -0.00125), and E^e plays a more critical role than $\sigma_{y_0}^{m}$ since $\sigma_{y_0}^{m}$ is in the logarithm. The second term in Eq. 12 reveals that electrolyte with a higher $\sigma_{y_0}^{e}$ (combined with a higher E^e, as $\log E^e$ needs to be greater than $\log \sigma_{y_0}^{e}$) can also inhibit the dendrite. When $\sigma_{y_0}^{e}$ is much smaller than 1MPa, it will promote the dendrite growth. The second term also explains that when $\sigma_{y_0}^{e}$ is small, increasing $\sigma_{y_0}^{m}$ (such that $\log \sigma_{y_0}^{m}$ becomes greater than $\log E^m$) will also result in a smaller dendrite length L. From Eq. 13, the area ratio (A%) is highly dependent on E^e. With a relatively higher E^e, the decrease of $\sigma_{y_0}^{e}$ and $\sigma_{y_0}^{m}$ tend to further reduce A%. The second term in Eq. 13 has limited effect on A% due to its much smaller coefficient (8.4×10^{-5}) compared to the first term in Eq. 13.

The dependence of dendrite morphology on the elastic modulus of the metal electrode (E^m) is complicated. From the first term in Eq. 12, with a lower $\sigma_{y_0}^{m}$ (e.g., smaller than 1MPa), the increase of E^m will increase the dendrite length. However, this reduction may be offset if the initial yield strength of the metal ($\sigma_{y_0}^{m}$) is high so that log $\tilde{\sigma}_{y_0}^{m}$ becomes positive. From Eq. 12, the side growth (area ratio) has less correlation with E^m, as E^m is only included in the second term of Eq. 13 with a much smaller coefficient (8.4×10^{-5}). It is noteworthy that the current model assumes the same Li metal electrochemical reaction kinetics while tuning the elastic modulus of the metal electrode. Therefore the results obtained from this machine learning model can only qualitatively predict the trend of dendrite growth for other metal electrode battery

systems.

Finally, we compare the values of the dendrite length and area ratio in the test datasets (not used for training the machine learning model), which are predicted from the machine learning (ML) model and calculated from the phase-field modeling (PFM). These results are plotted in Fig. 7(a), (c). It is seen that these datasets are clustered near a straight line, where the phase-field-calculated and machine-learning-predicted values are equal to each other. This indicates the machine learning model merits a good prediction to the dendrite morphology. The percentage of the prediction errors are plotted in Fig. 7(b) and (d), which reveal that most prediction errors are in the range of $\pm 20\%$. The DNN model results are as shown in Fig. S4. It shows that both prediction errors are also in the range of $\pm 15\%$ which is slightly better than SISSO results. However, the DNN model cannot output analytical equations, such as Eqs. 12, 13 from the SISSO model. With acceptable sacrifice of prediction accuracy, SISSO model is able to generate the direct connections between mechanical properties and dendrite growth which is easy to analyze.

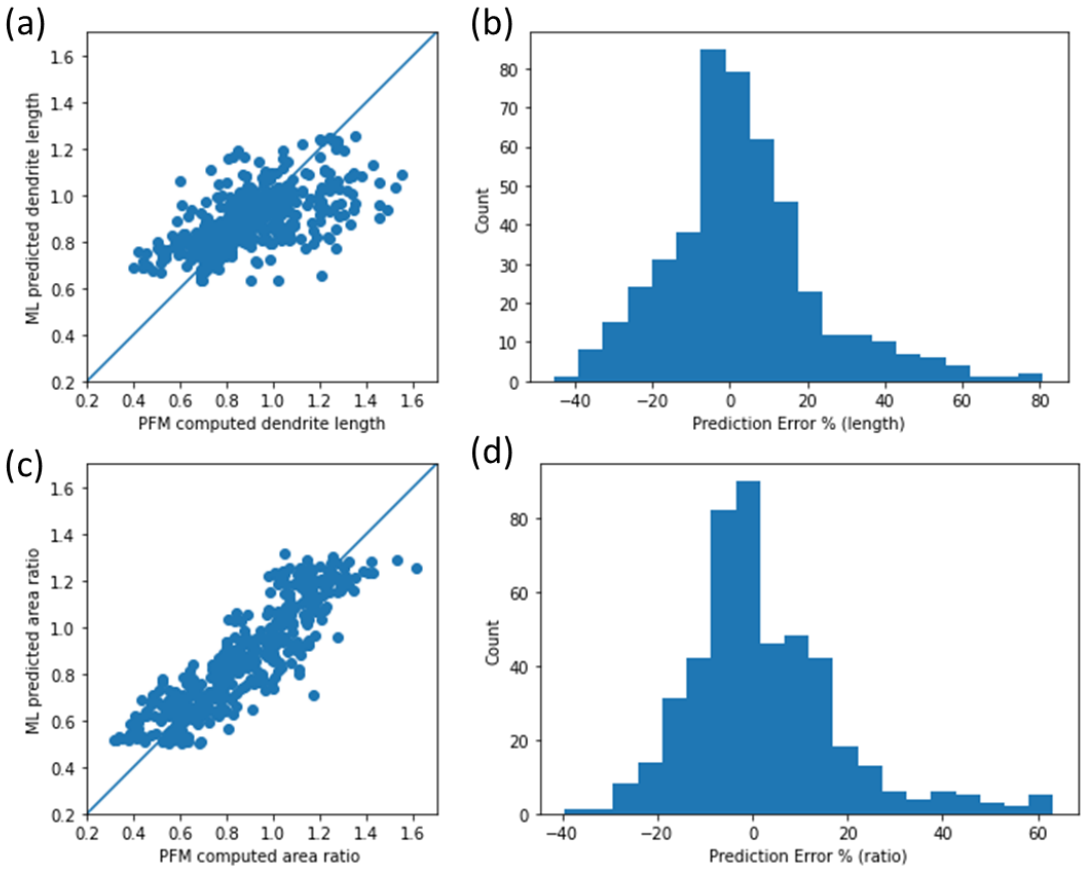

Figure 7 Comparisons of predicted values from SISSO model and true values from phase-field simulation for (a) dendrite length and (c) area ratio. Corresponding percentages of prediction error for (b) dendrite length and (d) area ratio.

5. Conclusion

In conclusion, a phase-field model coupled with solid mechanics module has been developed to simulate the electrodeposition process in solid state lithium metal battery system. The effects of the elastic and plastic mechanical properties of the Li metal and the solid electrolyte on Li dendrite growth are systematically investigated. It is revealed that electrolytes with high elastic modulus and initial yield strength can effectively inhibit the Li dendrite growth. This is because the high initial yield strength could help the electrolytes to endure higher deviatoric stresses that are induced by the higher elastic modulus, which eventually suppress the Li dendrite growth. Furthermore, increasing the initial yield strength of metal electrode could also lead to the dendrite inhibition in solid electrolytes of higher elastic modulus and lower initial yield strength. Finally,

high-throughput phase-field simulations are performed to explore the dependence of the Li dendrite morphology on the aforementioned mechanical properties of both the electrode and the electrolyte, and a machine learning model based on these high-throughput datasets yield interpretable analytical correlations between the materials properties and the dendrite morphology. This work thus provides a fundamental understanding of the mechanical inhibition effect on the dendrite growth in solid state batteries, and can potentially guide the selection and design of electrode and electrolyte materials for better suppression of dendrite growth.

AUTHOR INFORMATION

Corresponding Author

*Email: ye.cao@uta.edu

Author Contributions

Y.C. initiated and supervised the project. Y.R. performed the phase-field simulations. Y.R. and K.Z. did the machine learning part. Y.Z. did the experimental synthesis, testing, and characterization of the Li dendrite. Y.R. wrote the manuscript using feedback from Y.C. K.Z. and Y.Z..

Notes

The authors declare no competing financial interest.

SUPPORTING INFORMATION

Supporting information includes the experimental data for comparison with the simulation results, the phase-field simulation results of dendrite growth under different moduli which shows the elastic driving force and the summation of the remaining driving force, the different trends when the initial yield strength of metal changes and the machine learning results by neural network with better prediction accuracy.

ACKNOWLEDGMENTS

The work is supported by National Science Foundation (NSF) with Grant Nos. of NSF 2038083 (Y.R. & Y.C.) and NSF 2038082 (Y.Z.).

Reference

(1) Choi, J. W.; Aurbach, D. Promise and Reality of Post-Lithium-Ion Batteries with High Energy Densities. *Nat Rev Mater* **2016**, *1* (4), 16013. https://doi.org/10.1038/natrevmats.2016.13.

(2) Goodenough, J. B.; Park, K.-S. The Li-Ion Rechargeable Battery: A Perspective. *J. Am. Chem. Soc.* **2013**, *135* (4), 1167–1176. https://doi.org/10.1021/ja3091438.

(3) Kim, H.; Jeong, G.; Kim, Y.-U.; Kim, J.-H.; Park, C.-M.; Sohn, H.-J. Metallic Anodes for next Generation Secondary Batteries. *Chem. Soc. Rev.* **2013**, *42* (23), 9011. https://doi.org/10.1039/c3cs60177c.

(4) Armand, M.; Tarascon, J.-M. Building Better Batteries. *Nature* **2008**, *451* (7179), 652–657. https://doi.org/10.1038/451652a.

(5) Yang, C.; Fu, K.; Zhang, Y.; Hitz, E.; Hu, L. Protected Lithium-Metal Anodes in Batteries: From Liquid to Solid. *Adv. Mater.* **2017**, *29* (36), 1701169. https://doi.org/10.1002/adma.201701169.

(6) Zhang, W.; Nie, J.; Li, F.; Wang, Z. L.; Sun, C. A Durable and Safe Solid-State Lithium Battery with a Hybrid Electrolyte Membrane. *Nano Energy* **2018**, *45*, 413–419. https://doi.org/10.1016/j.nanoen.2018.01.028.

(7) Xu, W.; Wang, J.; Ding, F.; Chen, X.; Nasybulin, E.; Zhang, Y.; Zhang, J.-G. Lithium Metal Anodes for Rechargeable Batteries. *Energy Environ. Sci.* **2014**, *7* (2), 513–537. https://doi.org/10.1039/C3EE40795K.

(8) Cheng, X.-B.; Zhang, R.; Zhao, C.-Z.; Zhang, Q. Toward Safe Lithium Metal Anode in Rechargeable Batteries: A Review. *Chem. Rev.* **2017**, *117* (15), 10403–10473. https://doi.org/10.1021/acs.chemrev.7b00115.

(9) Abraham, K. M.; Jiang, Z. A Polymer Electrolyte-Based Rechargeable Lithium/Oxygen Battery. *J. Electrochem. Soc.* **1996**, *143* (1), 1–5. https://doi.org/10.1149/1.1836378.

(10) Manuel Stephan, A. Review on Gel Polymer Electrolytes for Lithium Batteries. *European Polymer Journal* **2006**, *42* (1), 21–42. https://doi.org/10.1016/j.eurpolymj.2005.09.017.

(11) Quartarone, E.; Mustarelli, P. Electrolytes for Solid-State Lithium Rechargeable Batteries: Recent Advances and Perspectives. *Chem. Soc. Rev.* **2011**, *40* (5), 2525. https://doi.org/10.1039/c0cs00081g.

(12) Mizuno, F.; Hayashi, A.; Tadanaga, K.; Tatsumisago, M. New, Highly Ion-Conductive Crystals Precipitated from Li2S-P2S5 Glasses. *Adv. Mater.* **2005**, *17* (7), 918–921. https://doi.org/10.1002/adma.200401286.

(13) Croce, F.; Appetecchi, G. B.; Persi, L.; Scrosati, B. Nanocomposite Polymer Electrolytes for Lithium Batteries. *Nature* **1998**, *394* (6692), 456–458. https://doi.org/10.1038/28818.

(14) Manuel Stephan, A.; Nahm, K. S. Review on Composite Polymer Electrolytes for Lithium Batteries. *Polymer* **2006**, *47* (16), 5952–5964. https://doi.org/10.1016/j.polymer.2006.05.069.

(15) Balazs, A. C.; Emrick, T.; Russell, T. P. Nanoparticle Polymer Composites: Where Two Small Worlds Meet. *Science* **2006**, *314* (5802), 1107–1110. https://doi.org/10.1126/science.1130557.
(16) Choi, J.-H.; Lee, C.-H.; Yu, J.-H.; Doh, C.-H.; Lee, S.-M. Enhancement of Ionic Conductivity of Composite Membranes for All-Solid-State Lithium Rechargeable Batteries Incorporating Tetragonal Li7La3Zr2O12 into a Polyethylene Oxide Matrix. *Journal of Power Sources* **2015**, *274*, 458–463. https://doi.org/10.1016/j.jpowsour.2014.10.078.
(17) Monroe, C.; Newman, J. The Impact of Elastic Deformation on Deposition Kinetics at Lithium/Polymer Interfaces. *J. Electrochem. Soc.* **2005**, *152* (2), A396. https://doi.org/10.1149/1.1850854.
(18) Cheng, E. J.; Sharafi, A.; Sakamoto, J. Intergranular Li Metal Propagation through Polycrystalline Li6.25Al0.25La3Zr2O12 Ceramic Electrolyte. *Electrochimica Acta* **2017**, *223*, 85–91. https://doi.org/10.1016/j.electacta.2016.12.018.
(19) Porz, L.; Swamy, T.; Sheldon, B. W.; Rettenwander, D.; Frömling, T.; Thaman, H. L.; Berendts, S.; Uecker, R.; Carter, W. C.; Chiang, Y. Mechanism of Lithium Metal Penetration through Inorganic Solid Electrolytes. *Adv. Energy Mater.* **2017**, *7* (20), 1701003. https://doi.org/10.1002/aenm.201701003.
(20) Li, Y.; Zhou, W.; Chen, X.; Lü, X.; Cui, Z.; Xin, S.; Xue, L.; Jia, Q.; Goodenough, J. B. Mastering the Interface for Advanced All-Solid-State Lithium Rechargeable Batteries. *Proc Natl Acad Sci USA* **2016**, *113* (47), 13313–13317. https://doi.org/10.1073/pnas.1615912113.
(21) Liu, Y.; Lin, D.; Yuen, P. Y.; Liu, K.; Xie, J.; Dauskardt, R. H.; Cui, Y. An Artificial Solid Electrolyte Interphase with High Li-Ion Conductivity, Mechanical Strength, and Flexibility for Stable Lithium Metal Anodes. *Adv. Mater.* **2017**, *29* (10), 1605531. https://doi.org/10.1002/adma.201605531.
(22) Liu, K.; Bai, P.; Bazant, M. Z.; Wang, C.-A.; Li, J. A Soft Non-Porous Separator and Its Effectiveness in Stabilizing Li Metal Anodes Cycling at 10 MA Cm $^{-2}$ Observed in Situ in a Capillary Cell. *J. Mater. Chem. A* **2017**, *5* (9), 4300–4307. https://doi.org/10.1039/C7TA00069C.
(23) Masias, A.; Felten, N.; Garcia-Mendez, R.; Wolfenstine, J.; Sakamoto, J. Elastic, Plastic, and Creep Mechanical Properties of Lithium Metal. *J Mater Sci* **2019**, *54* (3), 2585–2600. https://doi.org/10.1007/s10853-018-2971-3.
(24) Campbell, C.; Lee, Y. M.; Cho, K. Y.; Lee, Y.-G.; Lee, B.; Phatak, C.; Hong, S. Effect of Nanopatterning on Mechanical Properties of Lithium Anode. *Sci Rep* **2018**, *8* (1), 2514. https://doi.org/10.1038/s41598-018-20773-8.
(25) Xu, C.; Ahmad, Z.; Aryanfar, A.; Viswanathan, V.; Greer, J. R. Enhanced Strength and Temperature Dependence of Mechanical Properties of Li at Small Scales and Its Implications for Li Metal Anodes. *Proc Natl Acad Sci USA* **2017**, *114* (1), 57–61. https://doi.org/10.1073/pnas.1615733114.
(26) LePage, W. S.; Chen, Y.; Kazyak, E.; Chen, K.-H.; Sanchez, A. J.; Poli, A.; Arruda, E. M.; Thouless, M. D.; Dasgupta, N. P. Lithium Mechanics: Roles of Strain Rate and Temperature and Implications for Lithium Metal Batteries. *J.*

Electrochem. Soc. **2019**, *166* (2), A89–A97. https://doi.org/10.1149/2.0221902jes.
(27) Schultz, R. Fermilab-TM-2191; 2002; pp 1–6.
(28) Aguesse, F.; Manalastas, W.; Buannic, L.; Lopez del Amo, J. M.; Singh, G.; Llordés, A.; Kilner, J. Investigating the Dendritic Growth during Full Cell Cycling of Garnet Electrolyte in Direct Contact with Li Metal. *ACS Appl. Mater. Interfaces* **2017**, *9* (4), 3808–3816. https://doi.org/10.1021/acsami.6b13925.
(29) Wang, Y.; Cheng, Y.-T. A Nanoindentation Study of the Viscoplastic Behavior of Pure Lithium. *Scripta Materialia* **2017**, *130*, 191–195. https://doi.org/10.1016/j.scriptamat.2016.12.006.
(30) Ding, S.; Fairgrieve-Park, L.; Sendetskyi, O.; Fleischauer, M. D. Compressive Creep Deformation of Lithium Foil at Varied Cell Conditions. *Journal of Power Sources* **2021**, *488*, 229404. https://doi.org/10.1016/j.jpowsour.2020.229404.
(31) Zhang, L.; Yang, T.; Du, C.; Liu, Q.; Tang, Y.; Zhao, J.; Wang, B.; Chen, T.; Sun, Y.; Jia, P.; Li, H.; Geng, L.; Chen, J.; Ye, H.; Wang, Z.; Li, Y.; Sun, H.; Li, X.; Dai, Q.; Tang, Y.; Peng, Q.; Shen, T.; Zhang, S.; Zhu, T.; Huang, J. Lithium Whisker Growth and Stress Generation in an in Situ Atomic Force Microscope–Environmental Transmission Electron Microscope Set-Up. *Nat. Nanotechnol.* **2020**, *15* (2), 94–98. https://doi.org/10.1038/s41565-019-0604-x.
(32) Ren, Y.; Shen, Y.; Lin, Y.; Nan, C.-W. Direct Observation of Lithium Dendrites inside Garnet-Type Lithium-Ion Solid Electrolyte. *Electrochemistry Communications* **2015**, *57*, 27–30. https://doi.org/10.1016/j.elecom.2015.05.001.
(33) Yu, S.; Siegel, D. J. Grain Boundary Softening: A Potential Mechanism for Lithium Metal Penetration through Stiff Solid Electrolytes. *ACS Appl. Mater. Interfaces* **2018**, *10* (44), 38151–38158. https://doi.org/10.1021/acsami.8b17223.
(34) Yu, S.; Siegel, D. J. Grain Boundary Contributions to Li-Ion Transport in the Solid Electrolyte $Li_7La_3Zr_2O_{12}$ (LLZO). *Chem. Mater.* **2017**, *29* (22), 9639–9647. https://doi.org/10.1021/acs.chemmater.7b02805.
(35) Tian, H.-K.; Xu, B.; Qi, Y. Computational Study of Lithium Nucleation Tendency in Li7La3Zr2O12 (LLZO) and Rational Design of Interlayer Materials to Prevent Lithium Dendrites. *Journal of Power Sources* **2018**, *392*, 79–86. https://doi.org/10.1016/j.jpowsour.2018.04.098.
(36) Weston, J.; Steele, B. Effects of Inert Fillers on the Mechanical and Electrochemical Properties of Lithium Salt-Poly(Ethylene Oxide) Polymer Electrolytes. *Solid State Ionics* **1982**, *7* (1), 75–79. https://doi.org/10.1016/0167-2738(82)90072-8.
(37) Manthiram, A.; Yu, X.; Wang, S. Lithium Battery Chemistries Enabled by Solid-State Electrolytes. *Nat Rev Mater* **2017**, *2* (4), 16103. https://doi.org/10.1038/natrevmats.2016.103.

(38) Barai, P.; Higa, K.; Srinivasan, V. Effect of Initial State of Lithium on the Propensity for Dendrite Formation: A Theoretical Study. *J. Electrochem. Soc.* **2017**, *164* (2), A180–A189. https://doi.org/10.1149/2.0661702jes.
(39) Barai, P.; Higa, K.; Srinivasan, V. Impact of External Pressure and Electrolyte Transport Properties on Lithium Dendrite Growth. *J. Electrochem. Soc.* **2018**, *165* (11), A2654–A2666. https://doi.org/10.1149/2.0651811jes.
(40) Barai, P.; Higa, K.; Srinivasan, V. Lithium Dendrite Growth Mechanisms in Polymer Electrolytes and Prevention Strategies. *Phys. Chem. Chem. Phys.* **2017**, *19* (31), 20493–20505. https://doi.org/10.1039/C7CP03304D.
(41) Ahmad, Z.; Viswanathan, V. Stability of Electrodeposition at Solid-Solid Interfaces and Implications for Metal Anodes. *Phys. Rev. Lett.* **2017**, *119* (5), 056003. https://doi.org/10.1103/PhysRevLett.119.056003.
(42) Guyer, J. E.; Boettinger, W. J.; Warren, J. A.; McFadden, G. B. Phase Field Modeling of Electrochemistry. II. Kinetics. *Phys. Rev. E* **2004**, *69* (2), 021604. https://doi.org/10.1103/PhysRevE.69.021604.
(43) Liang, L.; Qi, Y.; Xue, F.; Bhattacharya, S.; Harris, S. J.; Chen, L.-Q. Nonlinear Phase-Field Model for Electrode-Electrolyte Interface Evolution. *Phys. Rev. E* **2012**, *86* (5), 051609. https://doi.org/10.1103/PhysRevE.86.051609.
(44) Liang, L.; Chen, L.-Q. Nonlinear Phase Field Model for Electrodeposition in Electrochemical Systems. *Appl. Phys. Lett.* **2014**, *105* (26), 263903. https://doi.org/10.1063/1.4905341.
(45) Chen, L.; Zhang, H. W.; Liang, L. Y.; Liu, Z.; Qi, Y.; Lu, P.; Chen, J.; Chen, L.-Q. Modulation of Dendritic Patterns during Electrodeposition: A Nonlinear Phase-Field Model. *Journal of Power Sources* **2015**, *300*, 376–385. https://doi.org/10.1016/j.jpowsour.2015.09.055.
(46) Yan, H. H.; Bie, Y. H.; Cui, X. Y.; Xiong, G. P.; Chen, L. A Computational Investigation of Thermal Effect on Lithium Dendrite Growth. *Energy Conversion and Management* **2018**, *161*, 193–204. https://doi.org/10.1016/j.enconman.2018.02.002.
(47) Hong, Z.; Viswanathan, V. Phase-Field Simulations of Lithium Dendrite Growth with Open-Source Software. *ACS Energy Lett.* **2018**, *3* (7), 1737–1743. https://doi.org/10.1021/acsenergylett.8b01009.
(48) Ren, Y.; Zhou, Y.; Cao, Y. Inhibit of Lithium Dendrite Growth in Solid Composite Electrolyte by Phase-Field Modeling. *J. Phys. Chem. C* **2020**, *124* (23), 12195–12204. https://doi.org/10.1021/acs.jpcc.0c01116.
(49) Tian, H.-K.; Liu, Z.; Ji, Y.; Chen, L.-Q.; Qi, Y. Interfacial Electronic Properties Dictate Li Dendrite Growth in Solid Electrolytes. *Chem. Mater.* **2019**, *31* (18), 7351–7359. https://doi.org/10.1021/acs.chemmater.9b01967.
(50) Yurkiv, V.; Foroozan, T.; Ramasubramanian, A.; Shahbazian-Yassar, R.; Mashayek, F. The Influence of Stress Field on Li Electrodeposition in Li-Metal Battery. *MRC* **2018**, *8* (03), 1285–1291. https://doi.org/10.1557/mrc.2018.146.
(51) Peled, E. The Electrochemical Behavior of Alkali and Alkaline Earth Metals in Nonaqueous Battery Systems—The Solid Electrolyte Interphase Model. *J.*

Electrochem. Soc. **1979**, *126* (12), 2047–2051. https://doi.org/10.1149/1.2128859.
(52) Zhang, S. S.; Xu, K.; Jow, T. R. EIS Study on the Formation of Solid Electrolyte Interface in Li-Ion Battery. *Electrochimica Acta* **2006**, *51* (8–9), 1636–1640. https://doi.org/10.1016/j.electacta.2005.02.137.
(53) Yurkiv, V.; Foroozan, T.; Ramasubramanian, A.; Shahbazian-Yassar, R.; Mashayek, F. Phase-Field Modeling of Solid Electrolyte Interface (SEI) Influence on Li Dendritic Behavior. *Electrochimica Acta* **2018**, *265*, 609–619. https://doi.org/10.1016/j.electacta.2018.01.212.
(54) Ouyang, R.; Curtarolo, S.; Ahmetcik, E.; Scheffler, M.; Ghiringhelli, L. M. SISSO: A Compressed-Sensing Method for Identifying the Best Low-Dimensional Descriptor in an Immensity of Offered Candidates. *Phys. Rev. Materials* **2018**, *2* (8), 083802. https://doi.org/10.1103/PhysRevMaterials.2.083802.
(55) Zhang, H.-W.; Liu, Z.; Liang, L.; Chen, L.; Qi, Y.; Harris, S. J.; Lu, P.; Chen, L.-Q. Understanding and Predicting the Lithium Dendrite Formation in Li-Ion Batteries: Phase Field Model. *ECS Transactions* **2014**, *61* (8), 1–9. https://doi.org/10.1149/06108.0001ecst.
(56) Mullin, S. A.; Stone, G. M.; Panday, A.; Balsara, N. P. Salt Diffusion Coefficients in Block Copolymer Electrolytes. *J. Electrochem. Soc.* **2011**, *158* (6), A619. https://doi.org/10.1149/1.3563802.
(57) Tariq, S.; Ammigan, K.; Hurh, P.; Schultz, R.; Liu, P.; Shang, J. LI Material Testing- Fermilab Antiproton Source Litihum Collection Lens. In *Proceedings of the 2003 Bipolar/BiCMOS Circuits and Technology Meeting (IEEE Cat. No.03CH37440)*; IEEE: Portland, OR, USA, 2003; Vol. 3, pp 1452–1454. https://doi.org/10.1109/PAC.2003.1288558.
(58) Geng, H.; Rosen, R.; Zheng, B.; Shimoda, H.; Fleming, L.; Liu, J.; Zhou, O. Fabrication and Properties of Composites of Poly(Ethylene Oxide) and Functionalized Carbon Nanotubes. *Adv. Mater.* **2002**, No. 19, 4.
(59) Moreno, M.; Quijada, R.; Santa Ana, M. A.; Benavente, E.; Gomez-Romero, P.; González, G. Electrical and Mechanical Properties of Poly(Ethylene Oxide)/Intercalated Clay Polymer Electrolyte. *Electrochimica Acta* **2011**, *58*, 112–118. https://doi.org/10.1016/j.electacta.2011.08.096.
(60) Monroe, C.; Newman, J. Dendrite Growth in Lithium/Polymer Systems. *J. Electrochem. Soc.* **2003**, *150* (10), A1377. https://doi.org/10.1149/1.1606686.
(61) Ichikawa, K.; Nozaki, H.; Komazawa, N.; Tachibana, A. Theoretical Study of Lithium Clusters by Electronic Stress Tensor. *AIP Advances* **2012**, *2* (4), 042195. https://doi.org/10.1063/1.4774037.
(62) Bower, A. F. *Applied Mechanics of Solids*, 0 ed.; CRC Press, 2009. https://doi.org/10.1201/9781439802489.
(63) Cheng, Q.; Wei, L.; Liu, Z.; Ni, N.; Sang, Z.; Zhu, B.; Xu, W.; Chen, M.; Miao, Y.; Chen, L.-Q.; Min, W.; Yang, Y. Operando and Three-Dimensional Visualization of Anion Depletion and Lithium Growth by Stimulated Raman

Scattering Microscopy. *Nat Commun* **2018**, *9* (1), 2942. https://doi.org/10.1038/s41467-018-05289-z.

(64) Sakuda, A.; Hayashi, A.; Takigawa, Y.; Higashi, K.; Tatsumisago, M. Evaluation of Elastic Modulus of Li_2S–P_2S_5 Glassy Solid Electrolyte by Ultrasonic Sound Velocity Measurement and Compression Test. *J. Ceram. Soc. Japan* **2013**, *121* (1419), 946–949. https://doi.org/10.2109/jcersj2.121.946.

(65) Herbert, E. G.; Tenhaeff, W. E.; Dudney, N. J.; Pharr, G. M. Mechanical Characterization of LiPON Films Using Nanoindentation. *Thin Solid Films* **2011**, *520* (1), 413–418. https://doi.org/10.1016/j.tsf.2011.07.068.

(66) Kasemchainan, J.; Zekoll, S.; Spencer Jolly, D.; Ning, Z.; Hartley, G. O.; Marrow, J.; Bruce, P. G. Critical Stripping Current Leads to Dendrite Formation on Plating in Lithium Anode Solid Electrolyte Cells. *Nat. Mater.* **2019**, *18* (10), 1105–1111. https://doi.org/10.1038/s41563-019-0438-9.

(67) Krauskopf, T.; Hartmann, H.; Zeier, W. G.; Janek, J. Toward a Fundamental Understanding of the Lithium Metal Anode in Solid-State Batteries—An Electrochemo-Mechanical Study on the Garnet-Type Solid Electrolyte $Li_{6.25}Al_{0.25}La_3Zr_2O_{12}$. *ACS Appl. Mater. Interfaces* **2019**, *11* (15), 14463–14477. https://doi.org/10.1021/acsami.9b02537.

(68) Wang, M. J.; Choudhury, R.; Sakamoto, J. Characterizing the Li-Solid-Electrolyte Interface Dynamics as a Function of Stack Pressure and Current Density. *Joule* **2019**, *3* (9), 2165–2178. https://doi.org/10.1016/j.joule.2019.06.017.

(69) Zhang, X.; Wang, Q. J.; Harrison, K. L.; Jungjohann, K.; Boyce, B. L.; Roberts, S. A.; Attia, P. M.; Harris, S. J. Rethinking How External Pressure Can Suppress Dendrites in Lithium Metal Batteries. *J. Electrochem. Soc.* **2019**, *166* (15), A3639–A3652. https://doi.org/10.1149/2.0701914jes.